Towards a universal molecular sensor: Self-assembled nanoparticle arrays for multi-phase trace analyte detection

Michael P. Cecchini,[‡&] Vladimir Turek,[‡&] Jack Paget,[‡] Alexei A. Kornyshev,*[‡] and Joshua B. Edel*[‡]

[‡]Department of Chemistry, Imperial College London, South Kensington Campus, London, SW7 2AZ

[&] These authors contributed equally to this publication

[*] Corresponding author: joshua.edel@imperial.ac.uk ; a.kornyshev@imperial.ac.uk

Abstract

Nanoplasmonic structures designed for trace analyte detection by surface enhanced Raman spectroscopy typically require sophisticated nanofabrication techniques. An alternative to fabricating such arrays is to rely on self-assembly of nanoparticles at liquid-liquid or liquid-air interfaces into close-packed arrays. The density of the arrays can be fine tuned by modifying the nanoparticle functionality, pH of the solution, and salt concentration. Importantly, these arrays are robust, "self-healing", reproducible, and extremely easy to handle. Herein, we report on the use of such platforms made of Au nanoparticles for detection of (multi)analytes from the aqueous, organic, or air phases. The total interfacial area of the Au array, at the liquid-liquid interface, is approximately 25 mm^2, making this platform ideal for small volume samples, low concentrations, and trace analytes. Importantly, the ease of assembly and rapid

detection makes this platform ideal for in-field sample testing of toxins such as explosives, drugs, or other hazardous chemicals.

Introduction

Various analytical techniques exist that can be used for molecular detection of pollutants[1,2], explosives[3-5], narcotics[6,7], and pesticides[8]. Often "real-samples" contain a complex mixture of compounds, which need to be quantified. Furthermore, they frequently also contain analytes dissolved in various phases (e.g air, organic, and aqueous). This makes identifying chemical species dissolved in multiple phases a real challenge. This problem becomes further amplified when trace analyte detection is required, as the signal from background molecules can swamp the signal from the analyte.

One technique that holds great promise in this regard is surface enhance Raman spectroscopy, an extremely sensitive technique that can be tailored to provide the detection of specific analytes through their unique vibrational fingerprints. The narrow linewidth of SERS spectra allows for multiple analyte detection within complex mixtures, including trace detection down to the single molecule level[9-11]. SERS is already an established technique to detect explosives[4,12,13], narcotics[14,15] and pesticides[16].

The enhancement of the Raman signal comes as a result of exciting localized surface plasmons within metallic nanostructures[17]. Increasing the signal strength further can be achieved by tailoring the metallic substrate, thereby lowering the limits of detection. Of particular note, are two-dimensional arrays of closely packed metallic **n**ano**p**articles (NPs) on a substrate[18] or metallic nanocavities[19-21]. These benefit from multiple hot spots being generated in a uniform fashion over a larger substrate area generating high signal enhancement[22] throughout the entire substrate. Various methods exist to fabricate such structures including lithographic[18,23,24] and chemical approaches[19]. Metallic structures can also be fabricated from self assembled non-metallic scaffolds[25]. However minimizing the gap between particles or cavities and the complexity of substrate preparation, while maximizing uniformity is crucial to maximizing the electromagnetic field enhancement[26,27]. Precise nanofabrication techniques capable of achieving these goals can be costly, time consuming and not scalable. Furthermore, most SERS

substrates are difficult to clean after use which is impractical for in-the-field applications. In this context, a disposable, self-assembled is highly advantageous for practical applications.

Among the self-assembly techniques which are available, templated-assembly is one of the most convenient methods to generate a 2-dimensional NP array[28]. To avoid assembly at the solid interface, which generally requires chemical treatment prior to assembly[29], NP films formed at the interface between two immiscible phases, such as a **l**iquid-**l**iquid **i**nterface (LLI) or **l**iquid-**a**ir **i**nterface (LAI), can be used[30,31]. The interfacial tension between such phases is reduced by the adsorption of NPs[32] which ultimately stabilizes the assembly[33,34].

Herein, we show a SERS sensor assembled at the LLI capable of trace dual phase-dual-analyte detection. We demonstrate the benefits of liquid-liquid systems to allow for either hydrophilic, hydrophobic, and/or amphiphilic molecules to be captured and detected either individually or simultaneously. The LLI self-assembles the NPs into an array of closely packed spheres creating a multitude of hotspots uniformly distributed within the detection volume and ensuring all captured analyte molecules are at the point of detection[35]. Finally a method for the detection of airborne analytes is also presented which is based on the conversion of a LLI to a LAI.

Self-assembly of the NPs at the LLI. The method used throughout this work is aimed towards a practical, in-the-field usable device. With this in mind, the SERS 'sensor' was made using cost-effective and simple methods that require no specialized equipment or qualified personnel. Self-assembly of a thin film of NPs at the LLI was achieved by vigorously shaking a 2 mL polypropylene tube for approximately 10 seconds consisting of 0.5 mL of 1,2-**di**chloro**e**thane (DCE) and a 0.5 mL aqueous solution. The aqueous solution consisted of 20 mM NaCl and Au NPs with a diameter of 43 ± 4 nm. The aspect ratio of the NPs was 1.35 ± 0.22 at a concentration of $4.35 \pm 0.02 \times 10^{10}$ particles per mL. Initially 16 nm particles were used; however the larger particles provided greater SERS intensities for the same

number of analytes dissolved in either the aqueous or organic phase (ESI). The physical steps towards generating a NP film at the LLI is shown in

Figure 1A(i-v) and Figure 1B (i-v). After shaking, the resulting emulsion quickly separated into two distinct phases with the formation of a thin layer of self-assembled NPs between the two phases. A golden reflection was observed at the DCE/water interface suggesting NP localization. While there are a number of alternative methods for NP assembly at the LLI, such as (m)ethanol addition[36,37] and electrochemistry[38,39], emulsification was used throughout this work due to its simplicity and cost effectiveness. Assembly of the NPs relies on the spontaneous diffusion-limited NP localization to the LLI as well as an increased efficiency of assembly with increasing ionic strength of the aqueous phase. The emulsification process played two key roles, the first being a reduction in the average distance between the NPs and the LLI, thereby speeding up the diffusion limited localization to the interface; while the second was a reduction of the average distance of the analytes to the LLI and hence the NPs, allowing efficient analyte capture.

The exact structure of the layers of NPs at the LLI is extremely difficult to assess; however, the 2D nature of the dried assembly is evident from SEM images (ESI). After thin-film formation, all but 50 μL of the aqueous phase was removed (Figure 1A(iv)). This step increases the particle density at the LLI resulting in an aqueous droplet being formed consisting of NPs at the perimeter. The total number of NPs in the sample was determined to be $1.74 \pm 0.05 \times 10^{10}$. The actual number of NPs assembled at the LLI was confirmed to be in the range of 1.39×10^{10} to 1.71×10^{10} as calculated by UV-Vis spectroscopy. To perform SERS measurements the sample was transferred onto a 130-160 µm thick coverslip (Figure 1A (v)) which resulted in the NPs forming a thin film (in this case the aqueous phase was below the NPs and the organic phase above). The diameter of the LLI interface once placed on the coverslip was approximately 5 mm. Importantly all measurements were recorded as single spectra with an acquisition time of 100 ms.

Analyte loading on the NPs. As a feasibility study, the reporter fluorophore **m**alachite **g**reen **i**so**t**h**io**c**yanate (MGITC) was used as the target analyte. This dye was chosen due the resonance enhancement that can be achieved since MGITC absorbs light near the 632.8 nm wavelength of excitation source used in the experiments which increases the intensity of the Raman signal. Furthermore, at low concentrations MGITC is soluble in both the aqueous and organic phases respectively. Therefore, MGITC was used to test the performance and assess whether the platform was capable of detecting analytes in either phase. The method of LLI formation in this case is identical to what is described above with the exception of analyte incorporation. This was simply performed by initially dissolving MGITC in the organic phase (prior to shaking) at varying initial concentrations ranging from 115 $\pm$ 14 pmole to 1.15 $\pm$ 0.37 fmole in 10-fold increments (Figure 1A (i-v)). At the highest MGITC concentration, there were approximately 4.03 $\pm$ 0.48 $\times 10^3$ dye molecules bound to 1 NP assuming all MGITC dissolved in solution was homogenously distributed across all NPs in solution. At the lowest concentration, there were on average 25 $\pm$ 12 NPs containing one MGITC molecule. Examples of the surface enhanced resonant Raman scattering (SERRS) spectra for these samples at the LLI are shown in Figure 1A (vi). As expected a decrease in analyte concentration resulted in a decrease in the total count intensity rate. For example, comparing the intensities of the 1170 cm^{-1} vibrational band for the 1.15 $\pm$ 0.23 pmole and 11.5 $\pm$ 3.2 fmole samples, the peak intensity decreased by 99%. Although even lower **l**imits **o**f **d**etection (LODs) were achieved, the spectra there were not reproducible, the variance in the detected signals affected, presumably, by random fluctuations in the morphology of the NP arrays or/and by defects in the NP-analyte conjugation. For practical purposes $\approx$10 fmole LOD was reached for reproducible SERS signals of MGITC dissolved in DCE. Similarly, a further experiment was performed with MGITC dissolved in the aqueous phase (Figure 1B (i-vi)). This showed a 10-fold improvement, with an LOD of 1.15 $\pm$ 0.30 fmole, when compared to the previous case. This is likely due to MGITC in the aqueous phase having a direct route in order to bind to the NPs.

To test the versatility and the sensitivity of the system, non-resonant analytes were also used. The first example was a water soluble analyte, **m**ercapto-5-**n**itro**b**enz**i**midazole (MNBI), Figure 2A. Concentrations down to 8.20 ± 1.81 pmole could be detected which equates to approximately 347 ± 63 MNBI molecules bound per NP. Compared to MGITC the LOD using MNBI was higher as a result of no resonance enhancement. We expect the binding efficiency to be similar between MGITC and MNBI, as both form strong bonds with the gold NPs. Finally, a DCE soluble analyte, 4-**m**ethoxy-**α-t**oluene**t**hiol (MATT) was used to quantify the detection limits of a non-resonant analyte dissolved in the organic phase. The spectra can be seen in Figure 2B. It is interesting to note that unlike analytes dissolved in the aqueous phase, the LOD was much higher, 323 ± 91 pmole. This is likely due to the different binding chemistry taking place across the phase boundary. For example, MNBI is able to bind to the NP's surface prior to the NP adsorbing to the LLI, whereas the majority of MATT will only bind once the NPs are assembled at the LLI.

In addition to MATT and MNBI, other analytes which either did not contain a thiol group or a phenyl group were detected as shown in Figure 3 for 2,4-Dinitrotoluene (DNT) and aniline dissolved in the organic phase, as well as cysteine and adenosine-5'-triphosphate (ATP) dissolved in the aqueous phase. The presence of an amine, phosphate, nitro or thiol moiety on the analyte leads to an affinity with the gold's surface. Furthermore, the high Raman cross-section of phenyl groups gives a more resolvable signal – for example despite the very high gold affinity of the thiol on cysteine, the absence of a phenyl produces a lower signal-to-noise spectrum when compared to the unthiolated ATP, DNT and aniline. This nicely demonstrates the versatility of the sensor with respect to detecting either weaker binders or analytes with weaker Raman cross sections. Additionally, these spectra show that the LLI does not adversely affect the sensor, as comparisons with literature[40-43]. In all cases the signal-to-noise ratio and sensitivity is as good (if not better) for these analytes at the LLI. A multitude of other analytes with differing functionalities were also detected, further highlighting the versatility of the sensor; the SERS spectra of these are shown in the ESI.

Simultaneous multi-phase analyte detection at the LLI. Successfully independently detecting analytes dissolved in either the water or organic phase using the same sensor design presented the opportunity for simultaneous **d**ual-**p**hase-**d**ual-**a**nalyte (DPDA) detection. From a sensor perspective, the unique ability to dress the NPs with analytes with different solubilities across multiple phases simultaneously offers a unique prospect in getting one step closer to building a universal sensor. Furthermore, from more of a chemical perspective, this multi-phase system can also be used to decorate a NP surface with both aqueous- and organic-phase soluble analytes simultaneously. This allows for direct control of not only the analyte type but the relative concentrations of different analytes on the NP surface. This is a significant advantage when compared to a solid-state substrate. Whilst solid-state substrates can potentially conjugate analytes from either phase, to detect both analytes, the conjugation processes would have to be separated. As such, there is little control over the relative analyte concentration on the NPs. Furthermore, the NPs on a solid-state surface are irreversibly bound, whereas a solution based system allows for the surface to be regenerated.

To characterize the LOD of simultaneous binding of analytes from both the organic and aqueous phases, the mole ratio of MNBI and MATT dissolved in each phase was precisely defined. MATT:MNBI was varied between 8.20 nmole:82 pmole (100:1) to 82.0 pmole:410 pmole (1:5). As an example, the effect of the mole ratio on the SERS intensity of the two analytes can be seen in Figure 4A-C, for mole ratios of 20:1, 2:1 and 1:5. In all spectra it is clear that the vibrational bands of both analytes could be seen and detected. For example, the 651, 1169, 1224, and 1604 cm^{-1} bands of MATT could easily be distinguished from the 1064, 1285, and 1333 cm^{-1} bands of NMBI. Furthermore, the relative intensities correlated nicely with the analyte concentration. While fluctuations in intensity did occur during the acquisition, the vibrational bands from both analytes resulted in equal enhancement which suggests their equal distribution across all NPs. The intensity of the MATT and MNBI vibrational bands were proportional to the concentration of each analyte dissolved in each phase. This was verified by comparing the average intensity ratio between the 1604 cm^{-1} vibrational band of MATT

and the 1333 cm^{-1} of MNBI (Figure 4D). Notably the mole ratio has been varied by over 3 orders of magnitude. Tri-analyte detection was also achieved and is described in the ESI.

Self-assembly of the NPs and analyte loading and detection at the LAI. A significant advantage of the system described in this manuscript relates to the possibility in converting the NPs embedded at a LLI to a LAI. This exciting prospect opens the door of using such a platform to also detect volatile or gaseous compounds. The LAI is simply produced by allowing the DCE phase at the LLI to evaporate. This process effectively removes the organic phase from the system whilst keeping the NPs at the aqueous-air interface. To test the capabilities of this platform, a 5 µL drop of pure MATT and aniline were placed inside an enclosed container together with the self-assembled NP film at the LAI. The separation between the LAI and analyte was 15 mm. A continuous, single-spot acquisition was performed on the interface, while adjusting the focal point to account for evaporation of the aqueous phase, using a 100 ms exposure time. The spectra of both analytes at 10, 25, 35, 83 and 180 seconds are shown in Figure 5. It is clear from the spectra that analyte capture can be achieved even for unthiolated analytes at the LAI. A time trace monitoring the intensity of the 1175cm^{-1} peak for MATT is shown in the ESI. The intensity shows a sharp increase within the first 60 s followed by a plateau indicating saturation of the analyte on the NP.

In conclusion, we have shown an alternative, highly sensitive analytical system based on a thin film NP array self-assembled at the LLI and LAI for trace analyte detection in various phases. The advantages of the sensor are numerous. An efficient capture mechanism is established by conjugating the NPs whilst they are still in bulk single particle dispersity. The conjugated NPs are quickly and effortlessly brought to the point of detection where they form into a thin film of closely packed nanospheres. Such a metallic film is perfect for SERS based detection as the space between closely packed spheres experience ultra-high electromagnetic field enhancement, increasing the SERS intensity and lowering the LOD.

A remarkable feature of the NP sensor at the LLI is the ability to detect multiple analytes dissolved in dual phases, which we have successfully demonstrated by detecting water-soluble and organic-phase-soluble molecules. Other thiolated and unthiolated molecules dissolved in either the water or organic phase were also detected with similar success. This versality in analyte detection eliminates the need for multiple devices, reducing analysis time and offering multiplexing capabilities. In addition to single phase analyte detection, the sensor has also shown the abilily to detect analytes dissolved both in the organic and aqueous phase simultaneously. The technique directly compares the SERS intensity of multiple analytes. We have shown that the mole ratios of both analytes play an important role in the SERS intensity of individual vibrational bands. Such a dependency allows direct comparison of mole ratios, using known and unknown analyte quantities. An additional advantage of the sensor is the ability to use it at the LAI to detect both thiolated and unthiolated airborne analytes.

It is probable that the LOD of the sensor could be reduced even further by adjusting the NP size, shape, tuning spacing, or changing the organic phase. We believe that this novel system opens vast possibilities for the in-field applications in various environmental, crime –prevention, anti-terror, and defense activities.

Methods

All analytes were purchase from Sigma-Aldrich and used without further purification. Chemicals used: 1,2-Dichloroethane (≥99.0%, ACS reagent); Methoxy-α-toluenethiol (90%, technical grade); 2-Mercapto-5-nitrobenzimidazole (97.0%); Sodium chloride (≥99.5%, puriss. p.a.); $HAuCl_4.\approx3H_2O$ (f.w. 339.79 (anhydrous), 99.999% trace metal basis); Trisodium citrate dihydrate (≥99%); 2,4-Dinitrotoluene (97%); L-cysteine (97%); Aniline (≥99.5%, ACS reagent); Adenosine 5'-triphosphate disodium salt hydrate (≥99%, Grade I). Ultra-pure water with a resistivity of 18.2 MΩ was used in all cases.

Nanoparticle Synthesis. Citrate stabilized Au NPs were synthesized using the Turkevich-Frens method[44,45]. The particles used in this work had an average hydrodynamic diameter of 64.7 ± 30.5 nm

with a polydispersity index (PDI) of 0.268 as measured using DLS. An extinction coefficient, ε_{max}, at 532 nm of $1.31 \times 10^{10}\,M^{-1}cm^{-1}$ [46] was used for 43 nm diameter NPs (from SEM). This value was used for all NP concentration evaluations using UV-Vis (ESI Figure 2). The concentration of the particles was adjusted using DI water for dilutions and centrifugation for concentration to a final working concentration of approximately 31.9 pM or 4.35×10^{10} NPs/mL. After the nanoparticles were assembled at the interface, the concentration of the aqueous bulk was measured. The difference between the initial nanoparticle concentration and the aqueous bulk was used to determine the number of particles located at the interface. Further details are included in the ESI.

Optical Configuration. SERS measurements were performed on a homebuilt Raman microscope[47]. Briefly, a 632.8 nm HeNe laser (HRP170, Thorlabs, 17 mW) excitation source was guided through two cleanup filters (LL01-633-12.5, Semrock) into an optical inverted microscope (IX71, Olympus). A linear polarizer (PRM1/M, Thorlabs) controlled the light polarization direction on the sample. The laser light was reflected into a 40x air objective (LUCPLANFLN, Olympus, NA 0.6, 4 mm WD) using a dichroic mirror (D1, LPD01-633RU-25x36x2.0, Semrock) mounted at a 45° angle of incidence. A long working distance objective was required to reach the NP assembly. The laser intensity at the sample was measured to be 8.5 mW using a digital power meter (PM100, Thorlabs). Backscattered light was collected through the same objective and transmitted through the same dichroic mirror. A long pass filter (LP1, LP02-633RU-25, Semrock) was used to reject the anti-Stokes scattered light and Rayleigh laser line. A Ø1" lens (LA1805-B, f = 30 mm, Thorlabs) focused the transmitted light onto the 50 μm entrance slit of the spectrograph (303 mm focal length, Shamrock SR-303i, Andor). The polychromatic light was then dispersed by a 600 l/mm grating (SR3-GRT-0600-0500, Andor) where it was imaged using an Electron Multiplying Charge Coupled Device (EMCCD, Newton DU970BV, Andor). All spectra were acquired using a 100 ms exposure time. The measurement was performed on the droplet and evaporation altered the optical pathway. Over the course of the acquisition, the stage position and focuse was manually adjusted to probe different areas of the substrate. At higher concentrations, signal

was emitted from all areas within the substrate. At lower dilutions, the uniformity in the signal intensity diminished, as the coverage of analyte with the probe volume was not uniform.

Analyte preparation

MGITC. 3 µL of 0.388 mM MGITC was dissolved in either 1000 µL of fresh DCE or water. 100 µL of this solution was added with 400 µL of the solvent (either water of DCE) providing 0.116 (±11.1-11.6%) nmole for detection (at the highest concentration). This was followed by 10-fold serial dilutions using 100 µL of the previous solution and diluting with 900 µL of the solvent. Again 100 µL were added to 400 µL of either the organic or aqueous phase for the subsequent sample. This dilution methodology was performed for all samples.

MATT. 5 µL of the organic soluble molecule, MATT, was initially diluted with 995 µL of DCE. 100 µL of this solution was added with 400 µL of fresh DCE providing 3.23 µmoles for detection. 10-fold serial dilutions followed using 100 µL of the previous dilutions sample and diluting with 900 µL of fresh DCE.

The solubility of MATT in water is calculated to be 0.74 g/L. The solubility of MATT in DCE or log $P_{DCE/wat}$ is not available, however the log $P_{oct/wat}$ is calculated to be 2.474 ± 0.238 (at 25 °C) and the polar surface area is 48.0 Å^2.* This means that the majority of the MATT will be dissolved in the hydrophobic (DCE) phase.
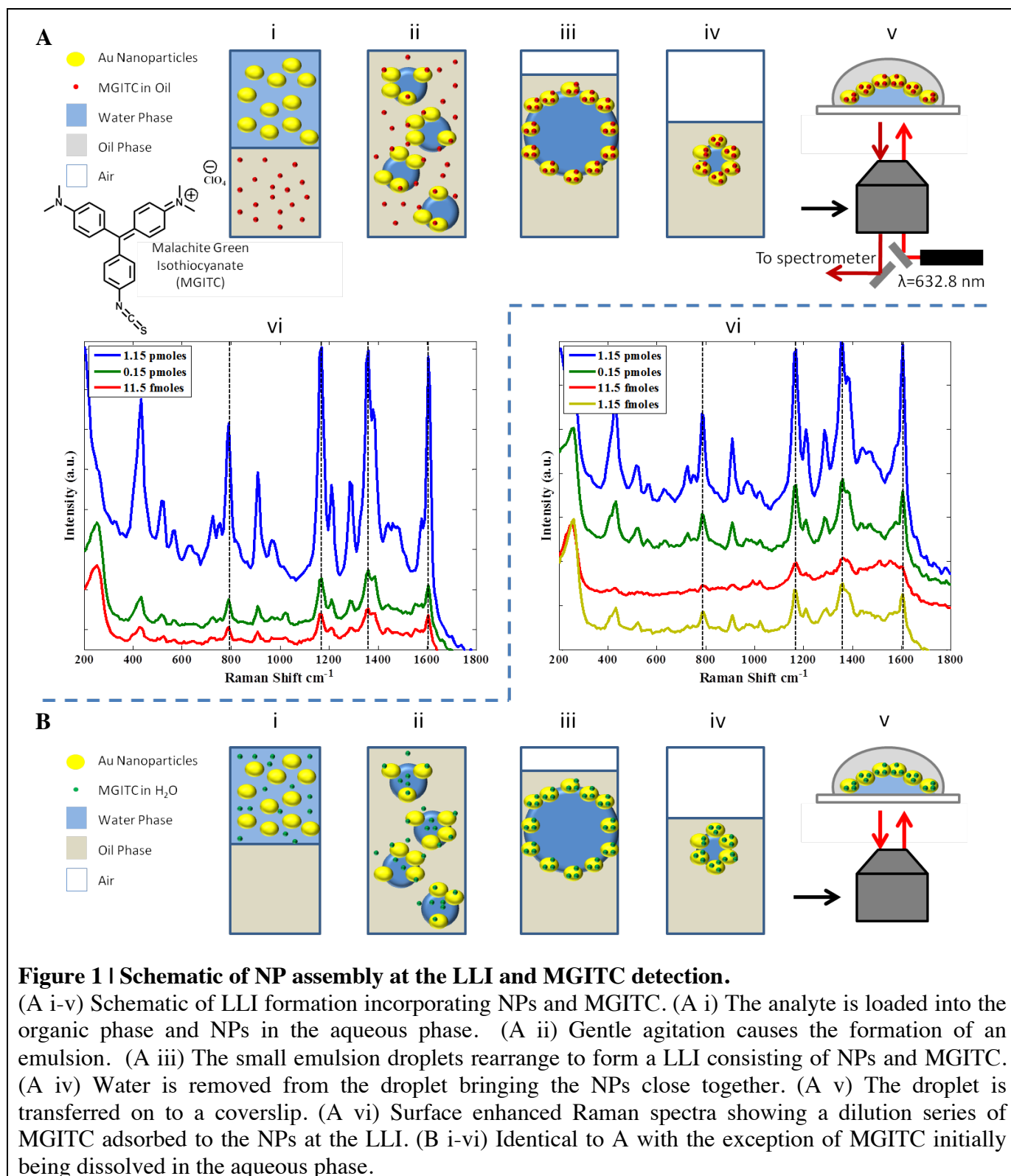
MNBI. Serial dilutions were performed using the stock analyte concentration and diluting with water. 0.16 mg 2-Mercapto-5-nitrobenzimidazole (MNBI, Sigma) was initially diluted with 10 mL of water. Subsequently, 100 µL of this was mixed with 400 µL of NPs. 10-fold serial dilutions followed using 100 µL of the previous sample and diluting with 900 µL of water. 100 µL of that was added to 400 µL of NPs.

The solubility of MNBI in water is calculated to be 0.43 g/L. The solubility of MNBI in DCE or log $P_{DCE/wat}$ is not available, however the log $P_{oct/wat}$ is calculated to be 1.404 ± 0.738 (at 25°C), while the polar surface area is 102 Å^2.* This means that MNBI is likely to have a greater mole fraction in water than MATT.

*Note: solubility, log P and polar surface area values for MATT and MNBI obtained through SciFinder – calculated by Advanced Chemical Development (ACD/Labs) Software V11.02 (© 1994-2012 ACD/Labs)).

Acknowledgements

Figure 1 | Schematic of NP assembly at the LLI and MGITC detection.
(A i-v) Schematic of LLI formation incorporating NPs and MGITC. (A i) The analyte is loaded into the organic phase and NPs in the aqueous phase. (A ii) Gentle agitation causes the formation of an emulsion. (A iii) The small emulsion droplets rearrange to form a LLI consisting of NPs and MGITC. (A iv) Water is removed from the droplet bringing the NPs close together. (A v) The droplet is transferred on to a coverslip. (A vi) Surface enhanced Raman spectra showing a dilution series of MGITC adsorbed to the NPs at the LLI. (B i-vi) Identical to A with the exception of MGITC initially being dissolved in the aqueous phase.
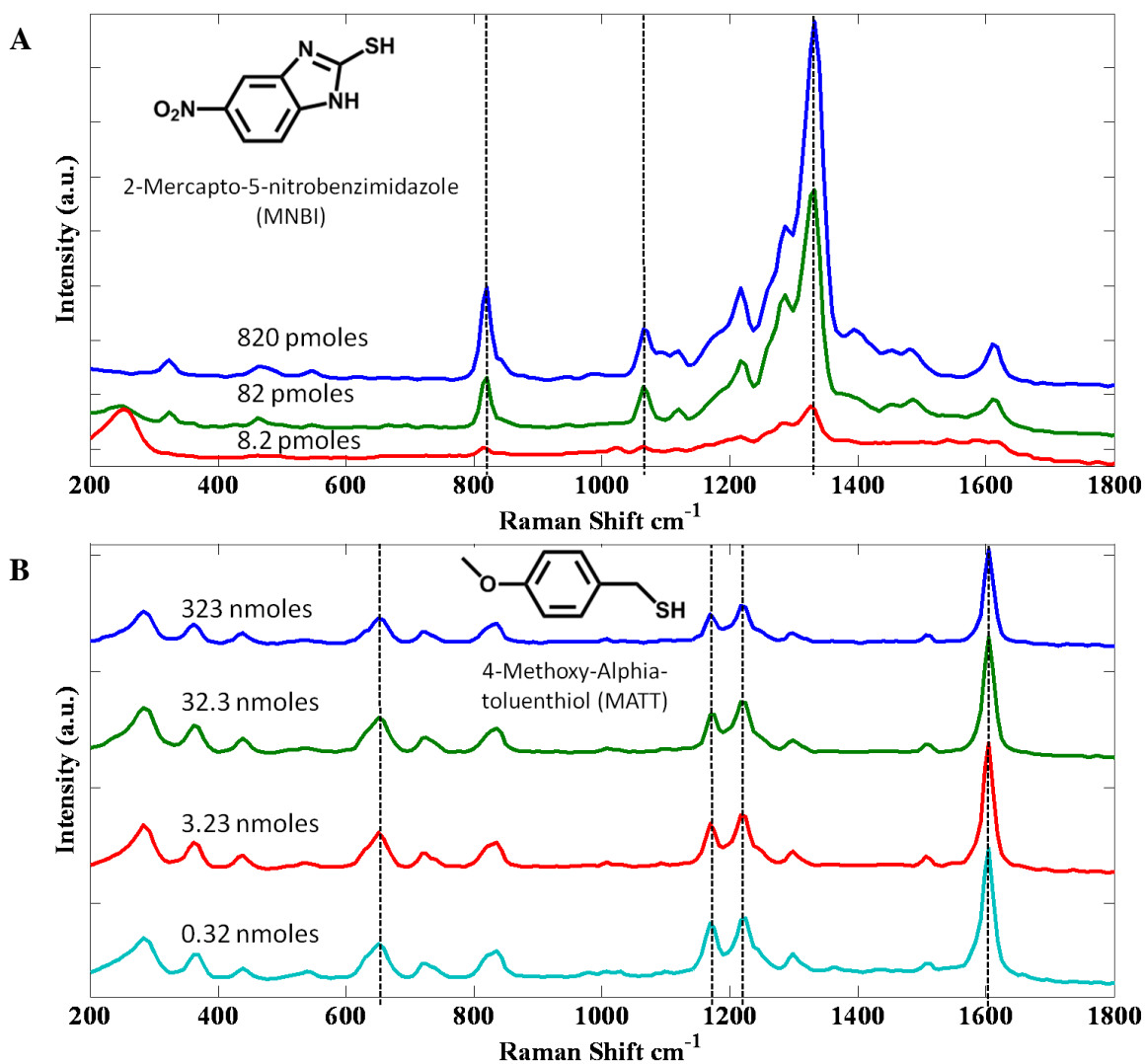
Figure 2 | Detection of analytes dissolved in the aqueous and organic interface.
(A) Surface enhanced Raman spectra showing a dilution series of MNBI adsorbed to the NPs at the LLI. Initially MNBI was dissolved in the aqueous phase. (B) Surface enhanced Raman spectra showing a dilution series of MATT adsorbed to the NPs at the LLI. MATT was initially dissolved in the organic phase.
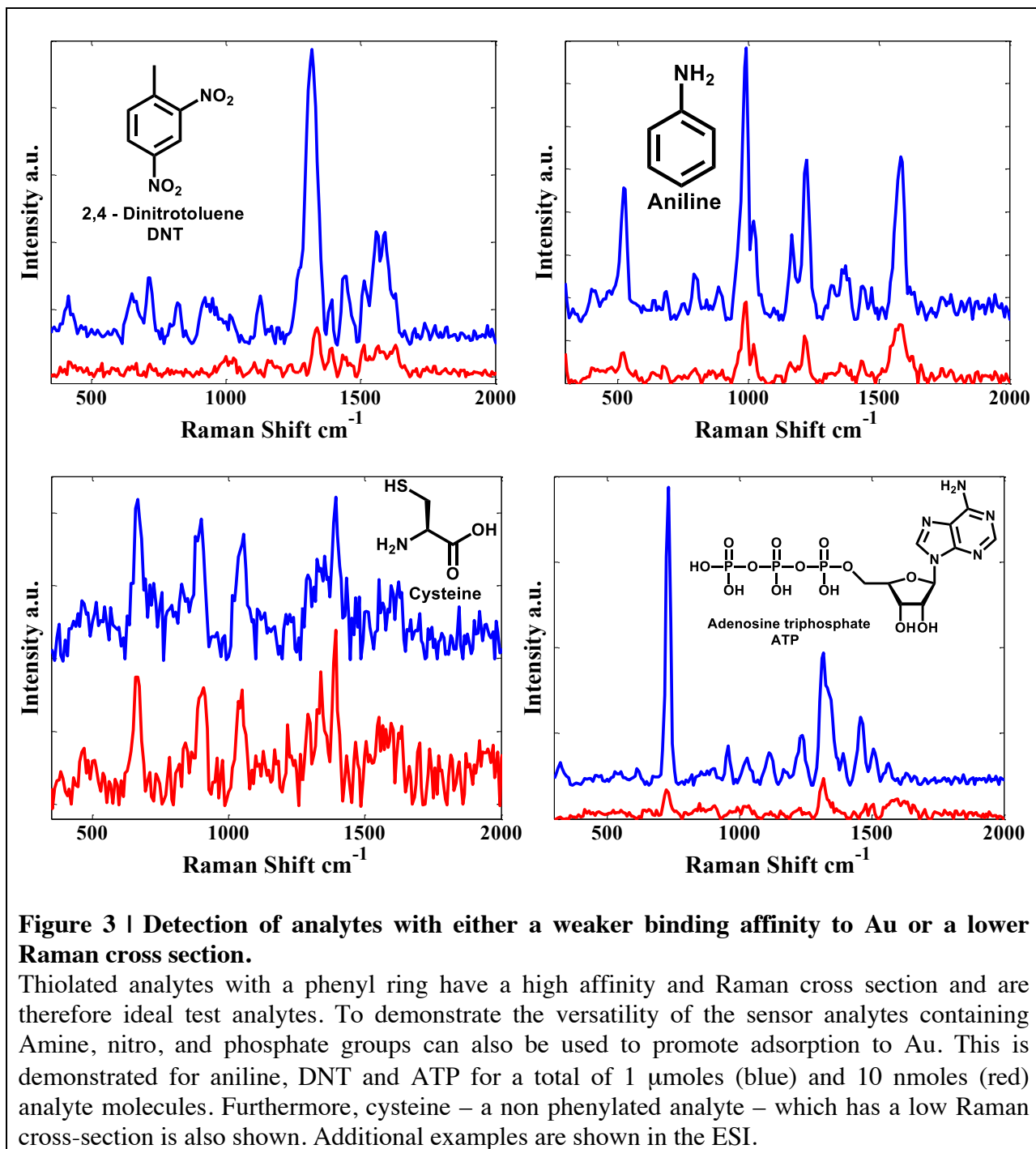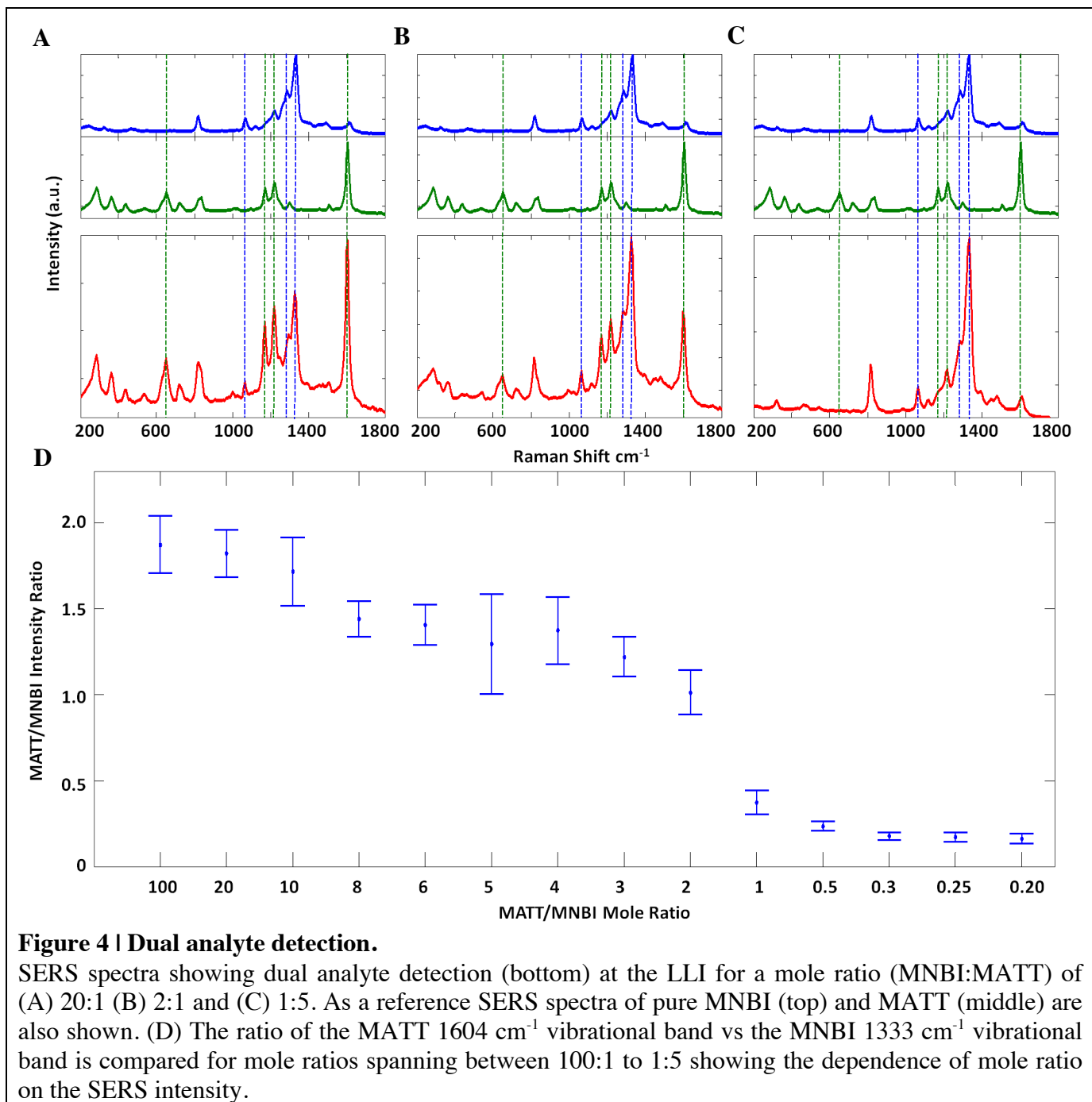
Figure 3 | Detection of analytes with either a weaker binding affinity to Au or a lower Raman cross section.

Thiolated analytes with a phenyl ring have a high affinity and Raman cross section and are therefore ideal test analytes. To demonstrate the versatility of the sensor analytes containing Amine, nitro, and phosphate groups can also be used to promote adsorption to Au. This is demonstrated for aniline, DNT and ATP for a total of 1 µmoles (blue) and 10 nmoles (red) analyte molecules. Furthermore, cysteine – a non phenylated analyte – which has a low Raman cross-section is also shown. Additional examples are shown in the ESI.
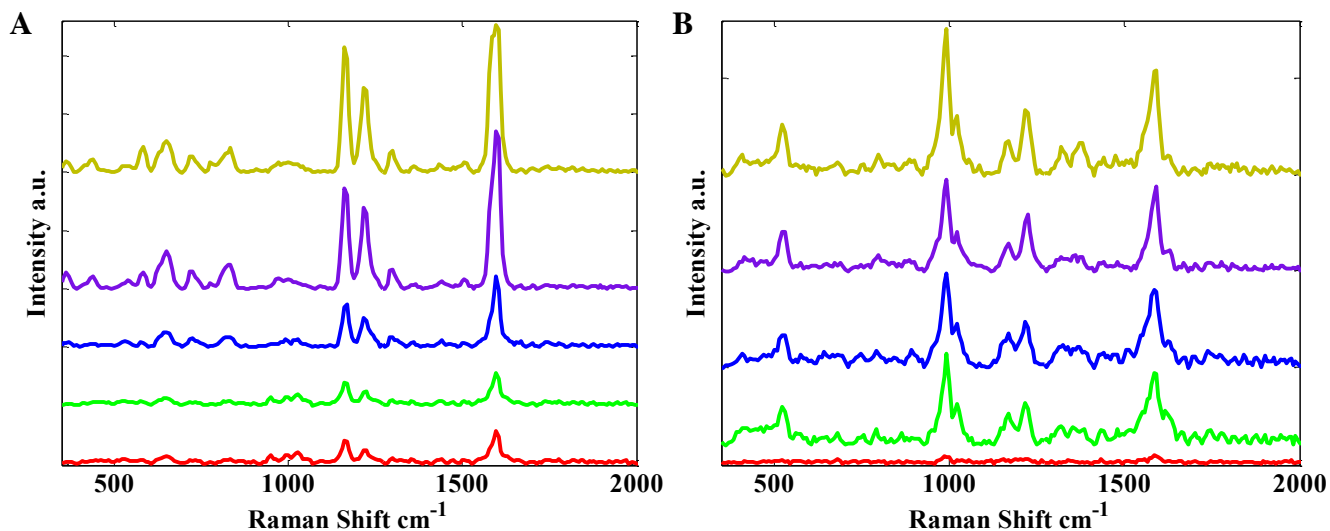
Figure 4 | Dual analyte detection.
SERS spectra showing dual analyte detection (bottom) at the LLI for a mole ratio (MNBI:MATT) of
(A) 20:1 (B) 2:1 and (C) 1:5. As a reference SERS spectra of pure MNBI (top) and MATT (middle) are
also shown. (D) The ratio of the MATT 1604 cm^{-1} vibrational band vs the MNBI 1333 cm^{-1} vibrational
band is compared for mole ratios spanning between 100:1 to 1:5 showing the dependence of mole ratio
on the SERS intensity.

Figure 5 | Airborne detection of MATT and Aniline at a liquid-air interface.
The same sensor capable of detecting analytes dissolved in the aqueous or organic phase can be used for airborne detection as well. After the sensor is assembled using the same method shown in Figure 1A (i-v) the DCE evaporates exposing the NPs to the air. Thiolated MATT (A) and unthiolated aniline (B) were placed 15 mm away from the interface. Full spectra snapshots at 10 s (red), 25 s (green), 35 s (blue), 83 s (purple) and 180 s (gold) over a single point on the interface show the increasing SERS intensity over time as a result of loading more analyte onto the nanopoarticles.

References

1   Lefevre, F. *et al*. Algal fluorescence sensor integrated into a microfluidic chip for water pollutant detection. *Lab on a Chip* **12**, 787-793 (2012).

2   Byer, R. L. & Garbuny, M. Pollutant Detection by Absorption Using Mie Scattering and Topographic Targets as Retroreflectors. *Appl. Opt.* **12**, 1496-1505 (1973).

3   Pushkarsky, M. B. *et al*. High-sensitivity detection of TNT. *Proceedings of the National Academy of Sciences* **103**, 19630-19634, doi:10.1073/pnas.0609789104 (2006).

4   Sylvia, J. M., Janni, J. A., Klein, J. D. & Spencer, K. M. Surface-enhanced raman detection of 2,4-dinitrotoluene impurity vapor as a marker to locate landmines. *Analytical Chemistry* **72**, 5834-5840 (2000).

5   Anderson, G. P. *et al*. TNT Detection Using Multiplexed Liquid Array Displacement Immunoassays. *Analytical Chemistry* **78**, 2279-2285, doi:10.1021/ac051995c (2006).

6   Kawano, R. *et al*. Rapid Detection of a Cocaine-Binding Aptamer Using Biological Nanopores on a Chip. *Journal of the American Chemical Society* **133**, 8474-8477, doi:10.1021/ja2026085 (2011).

7   Zhang, J. *et al*. Visual Cocaine Detection with Gold Nanoparticles and Rationally Engineered Aptamer Structures. *Small* **4**, 1196-1200, doi:10.1002/smll.200800057 (2008).

8   Liu, C. *et al*. Lateral Flow Immunochromatographic Assay for Sensitive Pesticide Detection by Using Fe3O4 Nanoparticle Aggregates as Color Reagents. *Analytical Chemistry* **83**, 6778-6784, doi:10.1021/ac201462d (2011).

9   Kneipp, K. *et al*. Single Molecule Detection Using Surface-Enhanced Raman Scattering (SERS). *Physical Review Letters* **78**, 1667 (1997).

10   Nie, S. & Emory, S. R. Probing Single Molecules and Single Nanoparticles by Surface-Enhanced Raman Scattering. *Science* **275**, 1102-1106, doi:10.1126/science.275.5303.1102 (1997).

11   Liu, H. *et al*. Single molecule detection from a large-scale SERS-active Au79Ag21 substrate. *Sci. Rep.* **1**, doi:http://www.nature.com/srep/2011/111010/srep00112/abs/srep00112.html#supplementary-information (2011).

12   Xu, J. Y. *et al*. SERS detection of explosive agent by macrocyclic compound functionalized triangular gold nanoprisms. *Journal of Raman Spectroscopy* **42**, 1728-1735, doi:10.1002/jrs.2932 (2011).

13   Yang, L., Ma, L., Chen, G., Liu, J. & Tian, Z.-Q. Ultrasensitive SERS Detection of TNT by Imprinting Molecular Recognition Using a New Type of Stable Substrate. *Chemistry – A European Journal* **16**, 12683-12693, doi:10.1002/chem.201001053 (2010).

14   Carter, J. C., Brewer, W. E. & Angel, S. M. Raman Spectroscopy for the in Situ Identification of Cocaine and Selected Adulterants. *Appl Spectrosc* **54**, 1876-1881, doi:10.1366/0003702001949014 (2000).

15   Bell, S. E. & Sirimuthu, N. M. Rapid, quantitative analysis of ppm/ppb nicotine using surface-enhanced Raman scattering from polymer-encapsulated Ag nanoparticles (gel-colls). *The Analyst* **129**, 1032-1036 (2004).

16   Shende, C., Gift, A., Inscore, F., Maksymiuk, P. & Farquharson, S. 1 edn (eds Bent S. Bennedsen *et al*.) 28-34 (SPIE).

17   Kelly, K. L., Coronado, E., Zhao, L. L. & Schatz, G. C. The Optical Properties of Metal Nanoparticles: The Influence of Size, Shape, and Dielectric Environment. *The Journal of Physical Chemistry B* **107**, 668-677, doi:10.1021/jp026731y (2002).

18   Yan, B. *et al*. Engineered SERS Substrates with Multiscale Signal Enhancement: Nanoparticle Cluster Arrays. *ACS Nano* **3**, 1190-1202, doi:10.1021/nn800836f (2009).

19   Chen, A. *et al*. Self-Assembled Large Au Nanoparticle Arrays with Regular Hot Spots for SERS. *Small* **7**, 2365-2371, doi:10.1002/smll.201100686 (2011).

20   Cintra, S. *et al*. Sculpted substrates for SERS. *Faraday Discussions* **132**, 191-199 (2006).

21   Mahajan, S., Baumberg, J. J., Russell, A. E. & Bartlett, P. N. Reproducible SERRS from structured gold surfaces. *Phys. Chem. Chem. Phys.* **9**, 6016-6020 (2007).

22   Dadosh, T. *et al*. Plasmonic Control of the Shape of the Raman Spectrum of a Single Molecule in a Silver Nanoparticle Dimer. *ACS Nano* **3**, 1988-1994, doi:10.1021/nn900422w (2009).

23   Kahl, M., Voges, E., Kostrewa, S., Viets, C. & Hill, W. Periodically structured metallic substrates for SERS. *Sensors and Actuators B: Chemical* **51**, 285-291, doi:10.1016/s0925-4005(98)00219-6 (1998).

24   Das, G. *et al*. Nano-patterned SERS substrate: Application for protein analysis vs. temperature. *Biosensors and Bioelectronics* **24**, 1693-1699, doi:10.1016/j.bios.2008.08.050 (2009).

25   Vignolini, S. *et al*. A 3D Optical Metamaterial Made by Self-Assembly. *Adv. Mater.* **24**, OP23-OP27, doi:10.1002/adma.201103610 (2012).

26   Hao, E. & Schatz, G. C. Electromagnetic fields around silver nanoparticles and dimers. *The Journal of chemical physics* **120**, 357-366 (2004).

27   Yang, Z.-L., Li, Q.-H., Ren, B. & Tian, Z.-Q. Tunable SERS from aluminium nanohole arrays in the ultraviolet region. *Chemical Communications* **47**, 3909-3911 (2011).

28   Grzelczak, M., Vermant, J., Furst, E. M. & Liz-Marzán, L. M. Directed Self-Assembly of Nanoparticles. *ACS Nano* **4**, 3591-3605, doi:10.1021/nn100869j (2010).

29   Liu, S., Zhu, T., Hu, R. & Liu, Z. Evaporation-induced self-assembly of gold nanoparticles into a highly organized two-dimensional array. *Physical Chemistry Chemical Physics* **4**, 6059-6062 (2002).

30   Boker, A., He, J., Emrick, T. & Russell, T. P. Self-assembly of nanoparticles at interfaces. *Soft Matter* **3** (2007).

31   Santos, H. A. *et al*. Electrochemical Study of Interfacial Composite Nanostructures: Polyelectrolyte/Gold Nanoparticle Multilayers Assembled on Phospholipid/Dextran Sulfate Monolayers at a Liquid–Liquid Interface. *The Journal of Physical Chemistry B* **109**, 20105-20114, doi:10.1021/jp052485p (2005).

32   Du, K., Glogowski, E., Emrick, T., Russell, T. P. & Dinsmore, A. D. Adsorption Energy of Nano- and Microparticles at Liquid–Liquid Interfaces. *Langmuir* **26**, 12518-12522, doi:10.1021/la100497h (2010).

33   Pickering, S. U. Emulsions. *Journal of the Chemical Society D: Chemical Communications* **91**, 2021 (1907).

34   Gordon, K. C., McGarvey, J. J. & Taylor, K. P. Enhanced Raman scattering from liquid metal films formed from silver sols. *The Journal of Physical Chemistry* **93**, 6814-6817, doi:10.1021/j100355a046 (1989).

35   Oh, M. K., Yun, S., Kim, S. K. & Park, S. Effect of layer structures of gold nanoparticle films on surface enhanced Raman scattering. *Analytica Chimica Acta* **649**, 111-116, doi:10.1016/j.aca.2009.07.025 (2009).

36   Li, Y.-J., Huang, W.-J. & Sun, S.-G. A Universal Approach for the Self-Assembly of Hydrophilic Nanoparticles into Ordered Monolayer Films at a Toluene/Water Interface. *Angewandte Chemie International Edition* **45**, 2537-2539, doi:10.1002/anie.200504595 (2006).

37   Luo, M. X., Song, Y. M. & Dai, L. L. Effects of methanol on nanoparticle self-assembly at liquid-liquid interfaces: A molecular dynamics approach. *J Chem Phys* **131**, doi:10.1063/1.3258344 (2009).

38   Su, B. *et al*. Reversible Voltage-Induced Assembly of Au Nanoparticles at Liquid|Liquid Interfaces. *Journal of the American Chemical Society* **126**, 915-919, doi:10.1021/ja0386187 (2003).

39   Flatté, M. E., Kornyshev, A. A. & Urbakh, M. Electrovariable Nanoplasmonics and Self-Assembling Smart Mirrors. *The Journal of Physical Chemistry C* **114**, 1735-1747, doi:10.1021/jp9083234 (2010).

40   Sauer, G., Brehm, G. & Schneider, S. Preparation of SERS-active gold film electrodes via electrocrystallization: their characterization and application with NIR excitation. *Journal of Raman Spectroscopy* **35**, 568-576, doi:10.1002/jrs.1186 (2004).

41   Kumar, G. V. P. *et al*. Hot Spots in Ag Core−Au Shell Nanoparticles Potent for Surface-Enhanced Raman Scattering Studies of Biomolecules. *The Journal of Physical Chemistry C* **111**, 4388-4392, doi:10.1021/jp068253n (2007).

42   Jing, C. & Fang, Y. Experimental (SERS) and theoretical (DFT) studies on the adsorption behaviors of l-cysteine on gold/silver nanoparticles. *Chem Phys* **332**, 27-32, doi:10.1016/j.chemphys.2006.11.019 (2007).

43   Khaing Oo, M. K., Chang, C.-F., Sun, Y. & Fan, X. Rapid, sensitive DNT vapor detection with UV-assisted photo-chemically synthesized gold nanoparticle SERS substrates. *Analyst* **136**, 2811-2817 (2011).

44   Turkevich, J. A study of the nucleation and growth processes in the synthesis of colloidal gold. *Discussions of the Faraday Society* **11**, 55 (1951).

45   Frens, G. Controlled nucleation for the regulation of the particle size in monodisperse gold suspensions. *Nature* **241**, 20 (1973).

46   Liu, X., Atwater, M., Wang, J. & Huo, Q. Extinction coefficient of gold nanoparticles with different sizes and different capping ligands. *Colloids and Surfaces B: Biointerfaces* **58**, 3-7, doi:10.1016/j.colsurfb.2006.08.005 (2007).

47   Cecchini, M. P., Stapountzi, M. A., McComb, D. W., Albrecht, T. & Edel, J. B. Flow-Based Autocorrelation Studies for the Detection and Investigation of Single-Particle Surface-Enhanced Resonance Raman Spectroscopic Events. *Analytical Chemistry* **83**, 1418-1424, doi:10.1021/ac102925h (2011).